AGU ADVANCING EARTH AND SPACE SCIENCE

Space Weather

RESEARCH ARTICLE
10.1029/2020SW002463

Assimilation of Sparse Continuous Near-Earth Weather Measurements by NECTAR Model Morphing

I. A. Galkin[1], B. W. Reinisch[1,2], A. M. Vesnin[1,3], D. Bilitza[4,5], S. Fridman[6], J. B. Habarulema[7], and O. Veliz[8]

[1]Space Science Laboratory, University of Massachusetts Lowell, Lowell, MA, USA, [2]Lowell Digisonde International, LLC, Lowell, MA, USA, [3]Institute of Solar-Terrestrial Physics, Irkutsk, Russia, [4]Department of Physics and Astronomy, George Mason University, Fairfax, VA, USA, [5]Space Physics Data Facility, NASA, GSFC, Greenbelt, MD, USA, [6]North-West Research Associates, Monterey, CA, USA, [7]South African National Space Agency, Hermanus, South Africa, [8]Instituto Geofisico del Peru, Jicamarca Radio Observatory, Lima, Peru

Key Points:
- A novel technique is presented for assimilating fragmentary sensor data to produce a global-scale space weather nowcast
- The technique iteratively transforms ("morphs") an underlying global climatology model into agreement with available sensor data
- The technique senses the inherent multiscale diurnal periodicity of geosystems to restore missing information over no-data regions

Correspondence to:
I. A. Galkin,
ivan_galkin@uml.edu

Citation:
Galkin, I. A., Reinisch, B. W., Vesnin, A. M., Bilitza, D., Fridman, S., Habarulema, J. B., & Veliz, O. (2020). Assimilation of sparse continuous near-Earth weather measurements by NECTAR model morphing. *Space Weather*, *18*, e2020SW002463. https://doi.org/10.1029/2020SW002463

Received 30 JAN 2020
Accepted 27 AUG 2020
Accepted article online 1 SEP 2020

Abstract Non-linear Error Compensation Technique with Associative Restoration (NECTAR) is a novel approach to the assimilation of fragmentary sensor data to produce a global nowcast of the near-Earth space weather. NECTAR restores missing information by iteratively transforming ("morphing") an underlying global climatology model into agreement with currently available sensor data. The morphing procedure benefits from analysis of the inherent multiscale diurnal periodicity of the geosystems by processing 24-hr time histories of the differences between measured and climate-expected values at each sensor site. The 24-hr deviation time series are used to compute and then globally interpolate the diurnal deviation harmonics. NECTAR therefore views the geosystem in terms of its periodic planetary-scale basis to associate observed fragments of the activity with the grand-scale weather processes of the matching variability scales. Such approach strengthens the restorative capability of the assimilation, specifically when only a limited number of observatories is available for the weather nowcast. Scenarios where the NECTAR concept works best are common in planetary-scale near-Earth weather applications, especially where sensor instrumentation is complex, expensive, and therefore scarce. To conduct the assimilation process, NECTAR employs a Hopfield feedback recurrent neural network commonly used in the associative memory architectures. Associative memories mimic human capability to restore full information from its initial fragments. When applied to the sparse spatial data, such a neural network becomes a nonlinear multiscale interpolator of missing information. Early tests of the NECTAR morphing reveal its enhanced capability to predict system dynamics over no-data regions (spatial interpolation).

1. Introduction

Dynamic processes within the Earth and its surrounding space environment resist their comprehensive specification because only fragmentary sensor data are readily available to describe their progression in sufficient detail. We concern ourselves with the common scenario of a ground-based observatory network that monitors its geosystem of interest with high accuracy and cadence, but with only at a limited number of locations around the globe. Research and application examples of such sparse sensor configuration arise in near-Earth remote-sensing systems for space weather nowcast, especially where the required instrumentation is complex and expensive.

We approach the problem of inferring the system state using spatially underdetermined observations from the point of so-called *compressive sampling* (Rani et al., 2018), a discipline of signal processing in which the complete, high-resolution data grid is represented by a partial set of values taken at strategically placed grid cells. The compressive sampling techniques are designed to detect and reflect inherent spatial features of the original dataset that can then be represented by only a small number of computed values, for example, coefficients of expansion to a suitable functional basis, with minimal or otherwise acceptable loss of accuracy. Similarly, we introduce a method for computing such coefficients that can be used to reconstruct the complete, global field of particular observed properties. The proposed method, Non-linear Error Compensation Technique for Associative Restoration (NECTAR), employs an underlying empirical model of the system to optimally capture most relevant knowledge of its inherent, quiet-time spatial/temporal features, and then smoothly transforms (i.e., *morphs*) the model into agreement with available observations at

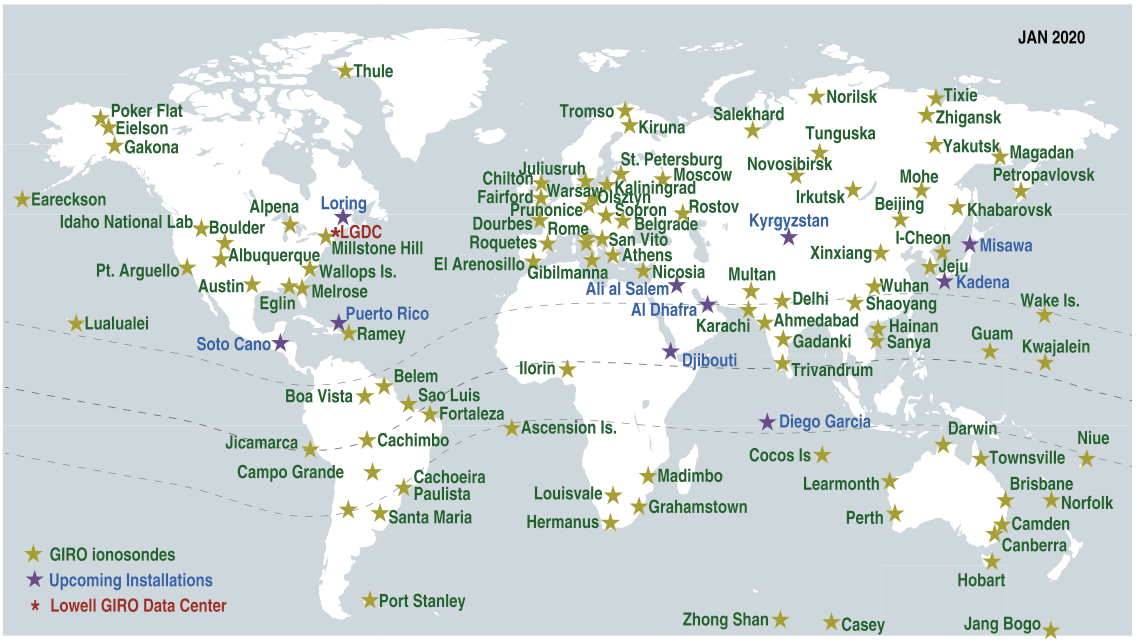

Figure 1. Global Ionosphere Radio Observatory (GIRO).

each time instance of data availability. The morphing operation preserves inherent features of the system through the model transformation process as it merely *adjusts* previously computed quiet-time coefficients. The cornerstone of NECTAR is a recurrent Hopfield neural network optimizer (Hopfield, 1982) that is responsible for smoothness of the transitions between the sensor-populated cells of the Earth grid to the global scale.

An important aspect of the NECTAR operation is its interpretation of geosystems in terms of diurnal harmonics of their variability within 24 hr: A system variable V at any geographic location (λ_G, ϕ_G) is viewed as a Fourier series on the hour angle T:

$$V(T,\lambda_G,\phi_G) = a_0(\lambda_G,\phi_G) + \sum_{i=1}^{H} a_i(\lambda_G,\phi_G)\cos iT + b_i(\lambda_G,\phi_G)\sin iT \quad (1)$$

where a_i and b_i are coefficients of the Fourier expansion of order H and the hour angle $T[°] = 15\ t[h] - 180$ ranges from 0 to 360. Such interpretation is especially fitting to the natural geosystems of periodic diurnal behavior (i.e., dependent on the Solar input), whose average behavior had been thoroughly studied in the past during coordinated worldwide multiyear observational campaigns to establish their climatology. Then less detailed real-time sensing must be arranged to obtain the minute-by-minute "weather" nowcast via data assimilation. This is the *empirical assimilative modeling* that (a) captures the essence of available sensor data, without imposing an underlying theoretical framework upon their representation, and (b) in accordance to the space weather model classification by Tsagouri et al. (2013), focuses on the operational nowcast scenarios that demand rapid assessment of the impact that space weather may bear on humans and technological systems in space.

This paper discusses key concepts of the NECTAR model morphing algorithm with examples of its application to the real-time assimilative modeling of Earth's ionosphere, the partially ionized region of the atmosphere ranging from ~50 to 2,000 km altitude, as it responds to anomalous grand-scale events in the Sun-Earth system that force the ionospheric plasma beyond its quiet-time behavior. The demonstration NECTAR-based ionosphere model is a follow-on from an earlier conceptual *Real-Time IRI* investigation by Galkin et al. (2012). Like before, we still use the International Reference Ionosphere (IRI) model (Bilitza, 1990; Bilitza et al., 2017, and references therein) as the underlying climate model, with its highly specialized set of diurnal and spatial expansion basis functions. Also, online continuous near real time ground-based sensors of the Global Ionosphere Radio Observatory (GIRO) (Reinisch & Galkin, 2011) are used, now expanded to include over 60 observatories operating in 30 countries (Figure 1). The NECTAR

algorithm has now implemented the early conceptual ideas to obtain high resolution global timelines of ionospheric behavior through occurring space weather events.

2. Motivation

Space weather as a discipline has been following the successful path of its meteorological counterpart with various implementations of the recursive Kalman filter (e.g., Ghil et al. (1981) and reference therein) in the framework of a theoretical "first-principles" model of the system. During the update step of the Kalman filter, the underlying model is brought into agreement with observations by manipulating the model drivers, therefore not only gleaning the system nowcast from the available observations, but also producing a self-consistent physics-based description of the processes that constitute the system. The update-operation usually matches the model only to the latest (near-real-time) measurements, in which case the update step does not involve the time dimension and in the general sense corresponds to the 3D variational form of assimilation, called 3D-Var or 3DDA (Lorenc, 1986). Computations that involve periods of past observations in the update process to estimate the system trajectory in time, that is, 4DDA techniques, have a proven track record of superior performance (e.g., Gauthier et al., 2007), though at a significantly greater demand for computer resources and algorithm complexity. Next, during the forecast step of the Kalman filter, the thus updated theoretical model is advanced one step into the future, forming the starting point for the next update step computations.

While a Kalman filter applied to a physics-based model has been highly successful in terrestrial weather applications, it has been facing significant challenges in its implementation for the space weather domain (McNamara et al., 2008), known for its complexity of dynamically coupled constituent systems (Sun, interplanetary space, magnetosphere, plasmasphere, ionosphere, and atmosphere): sensitivity to external drivers in the Sun-Earth realm, uncertainty of the sensor measurements because of inherent noise and biases, and, ultimately, the scarceness of observations useable for timely space weather reports. In particular, we are faced with the problem that at low and high latitudes where spatial gradients are the largest the station density is the thinnest. More crucially, the ionosphere demonstrates a near-immediate response to changes in its drivers, such that the prior state does not effectively inform the future state of the system. Furthermore, much like in the meteorological community, our most abundant observations are of parameters (i.e., plasma density) that do not significantly affect the future state of the system.

Since the full-physics Kalman filter for space weather is incurring substantial implementation time and effort expenses (Schunk et al., 2020), we looked for a high-accuracy weather specification via simpler model architectures that can take advantage of the 4DDA treatment of the problem.

3. Empirical Expansion Models

Empirical models capture the average essence of system behavior by representing historical data as a compact set of expansion coefficients into a suitable functional basis such as spherical and diurnal harmonics. Once the coefficients are computed from the available observations (the model is *trained*), the result can be used to predict such on-average system conditions for any given time and location. Choice of the optimal expansion basis is driven by arguments of minimizing the representation error, compacting the coefficient set, simplifying the computations, protecting the model against *overtraining* (i.e., representing data-specific rather than system-generic properties), and improving so-called "goodness of inductive bias," a capability to induce most characteristic features from available data (Mitchell, 1980). Over decades of empirical model developments, the expansion basis toolkit has been enriched with a great variety of techniques tailored to specific data domains so as to enhance their inductive bias. The morphing principles of NECTAR will be illustrated here on a particular example of the Jones and Gallet (1962) expansion basis, originally designed in the early 1960s as a part of the concerted efforts at the U.S. National Oceanic and Atmospheric Administration (NOAA) to build the 4-D ionospheric electron density distribution model. The Jones-Gallet basis was used to capture monthly median timelines of the O-polarization critical frequency of the F2 layer, f_oF2 (e.g., Davies, 1990), a commonly observed characteristic of the ionospheric plasma distribution that specifies the maximum density of ionospheric plasma, $NmF2\ [\mathrm{m}^{-3}] = 1.24 \times 10^{10} \times (f_o\mathrm{F2}\ [\mathrm{MHz}])^2$.

The Jones-Gallet basis is one of the early designs coined in the early 1960s that considered above optimized selection criteria in a strict and systematic way. In its general representation, it combines expansions over the "diurnal" basis D_i and the "geographic" basis G_k to define the quiet-time diurnal variation of the ionospheric f_oF2 characteristic as a function of time t and geographic location (λ_G, ϕ_G):

$$f_0F2(t, \lambda_G, \phi_G) = \sum_i \sum_k c_{ik} D_i(T) G_k(\lambda_G, \phi_G). \tag{2}$$

The Jones-Gallet expansion does not attempt to represent the seasonal variability of ionospheric features, nor the 11-year cyclic dependence on the ionization efficiency of the Sun. Instead, the coefficients c_{ik} in Equation 2 are computed and permanently stored separately for each of the 12 months for two levels of the solar activity (given by the 12-month smoothed sunspot number R_{12} of 0 and 100). Thus, the complete climatology of the ionosphere for any time and location requires 24 sets of coefficients. For a given time t, two sets of coefficients for the low/high levels of R_{12} for a given month are retrieved first, and then the c_{ik} are interpolated for specific R_{12} computed for the time of interest. The diurnal expansion over $D_i(T)$ basis in Equation 2 describes one "day in the life" (DITL) as a function of UT hour angle T, Equation 1. The geographic basis $G_k(\lambda_G, \phi_G)$ is a highly customized spatial non-harmonic functional basis built to optimally represent the ionospheric dependency on the geomagnetic field (see ITU-R (2009) for further detail):

$$\begin{aligned}
&G_k(\lambda_G, \phi_G) = F_n(\lambda_G, \phi_G) \cdot P_m(\lambda_G) \cdot L_m(\phi_G) = (\sin_\chi)^n \cdot (\cos \lambda_G)^m \cdot \begin{bmatrix} \cos m\phi_G \\ \sin m\phi_G \end{bmatrix}, \\
&\chi(\lambda_G, \phi_G) = \arctan\left(\frac{I(\lambda_G, \phi_G)}{\sqrt{\cos \lambda_G}}\right), \\
&m = 0, 1, ..., 8, \\
&n(m) = \{11, 11, 8, 4, 1, 0, 0, 0, 0\}.
\end{aligned} \tag{3}$$

$F_n(\lambda_G, \phi_G)$ represents the dependence of f_oF2 on the geomagnetic field, in particular, its Appleton anomaly about the magnetic equator, expressed as the power of sine function of the modified dip (modip) angle χ (Rawer, 1963), a function of the B-field dip angle $I(\lambda_G, \phi_G)$. The modip angle χ helps to reduce the contribution of $F_n(\lambda_G, \phi_G)$ towards the poles, where $P_m(\lambda_G)$ captures solar drivers of f_oF2 variation in the geographic latitude λ_G; powers of cosine are used in $P_m(\lambda_G)$ to suppress unstable expansion over the poles (Jones & Gallet, 1962). $L_m(\phi_G)$ uses conventional harmonics of ϕ_G to describe the latitudinal dependencies. Selection of orders for various terms in G_k was carefully optimized for f_oF2 to avoid the model over-training and contributions from the data noise. With m and $n(m)$ as defined in Equation 3, the total number of G_k terms for f_oF2 model is 76.

At each update step of NECTAR the empirical model formalism $D_i(T)G_k(\lambda_G, \phi_G)$ is kept unchanged, and the original expansion coefficients c_{ik} are adjusted to minimize differences between observations and model. The adjusting computation is designed carefully so as to preserve the characteristic features that were originally captured by training the climatology model. The outcome of this assimilation process is a continuous stream of updated coefficient sets, each computed at the cadence of the incoming new observational data. Because the computational expense of the adjustment operation is low in comparison to the full physics-based computation, the 4DDA assimilation algorithms—involving 24 hr of past observations rather than only the latest snapshot—are therefore feasible for implementation on desktop-quality computers. With this approach, it also becomes easier to disseminate the updated model state to the end users: the server-client interface now operates with significantly smaller data messages in comparison to the prohibitively voluminous data grids.

The empirical and physics-based approaches are in fact complementary: The physics-based assimilation describes the system state in terms of many coupled processes that are responsible for the model outcome, while the empirical assimilation is capable of representing events that are yet to be understood and described theoretically. Contrasting two types of models applied to the same sensor data is a powerful investigative tool to explore the unknowns of the geosystem behavior.

4. Interpolation Through Data Gaps and Errors

4.1. General Considerations

In the model-morphing approach to assimilation, the update step outcome is no longer the computation of the physics-based model driven by the optimal set of driving parameters. Instead, it is an expansion to a functional basis that minimizes the observation-model *differences*. As such, the morphing procedure is prone to the usual weaknesses of expansion computations over no-data areas in time and space, where unconstrained expansion can produce physically unreasonable, and in particular, oscillating representations of the missing data, for example, Rice (1993). Introduction of *phantom points* whose purpose is to constrain the expansion to a reasonable behavior is one possibility of avoiding such problems (Jones & Gallet, 1962; Reithinger et al., 2008). Addition of the phantom points is not a straightforward operation: missing data have to be derived with a careful consideration of the system constitution and behavior. For example, the phantom points for computation of the original f_oF2 expansion coefficients (Jones et al., 1969) were obtained using propagation of the same observed value in time along the line of constant modip angle (so-called "CCIR" specification detailed in ITU-R, 2009). Years later, this technique was revised by Rush et al. (1989) to account for the underlying aeronomy processes that affect the ionospheric plasma as the modip-driven propagation crosses the land-ocean boundary. Alternatively, ensuring that the morphing process is *elastic* is another possibility that we will discuss in subsequent publications on the topic.

Adding phantom points to the observational data in order to constrain the expansion process has been a common, though controversial approach. By design, the model-morphing method avoids much of the usual "interpolation" criticism by treating the data gap filling task in the framework of diurnal deviation harmonics that describe *differences* between observation and model. In this process, the interpolation procedure operates with the natural constituent processes in the ionosphere that exhibit a cyclic behavior of various scales.

First, we analyze time series of differences between observation and model at each sensor location to determine the diurnal deviation harmonics.

4.2. Single-Site Expansions

In the description of the time domain processing, we refer to time of validity t_v, usually associated with the time of the last coordinated sensor measurement used in the assimilation. In practice, the model computation and release happen a few minutes later than t_v because of various associated latencies of data acquisition and delivery to the central node for processing. Once the latest observations are retrieved from the network, 24-hr histories prior to t_v are assembled for each available sensor location. The 24-hr history is used to compute the local diurnal harmonics of the differences $\Delta V(t) = V_{obs}(t) - V_{mod}(t)$ timeline for $t_v - 24 < t < t_v$, where V_{obs} and V_{mod} are the observed and background model values, respectively. However, the original expansion formalism for the average "day in the life" representation, Equation 1, is not optimal for describing the weather dynamics $\Delta V(t)$ over a 24-hr period, since it assumes a periodic variation with a fundamental frequency of 1/24 [h^{-1}]. To consider the day-to-day variability of the measured $V(t)$, a linear *trend term* $\Delta b_0 t$ has therefore been added to the diurnal expansion of $\Delta V(t)$:

$$\Delta V(t) = \Delta a_0 + \Delta b_0 t + \sum_{i=1}^{H} \Delta a_i \cos iT + \Delta b_i \sin iT \quad (4)$$

Such linear term addition is not representative of the real trends in $\Delta V(t)$ and neither it will be optimal in projecting system behavior to future time. While higher orders of expansion are possible here, they will not principally enhance the temporal prediction capability of this approach; as we argued previously, the ionosphere tends to react to its drivers too rapidly to capture its future timeline from the prior state only. The main purpose of adding $\Delta b_0 t$ term here is to break the constraint of the climatological "day-in-the-life" Equation 1 that enforces smooth wrap-around of the time series back to $t_v - 24$ and therefore precludes the original expansion from accurately representing $\Delta V(t)$ at the nowcast t_v.

The linear *detrending* operation is applied first to determine Δb_0 before the Fourier decomposition is performed. Similar to Equation 1, Δa_i and Δb_i are the computed expansion coefficients, T is the UT hour angle with t ranging from $t_v - 24$ h to t_v, cos iT and sin iT are diurnal basis functions, and H is the order of expansion used for the empirical background formulation. Similar concepts can be found in other "weather versus

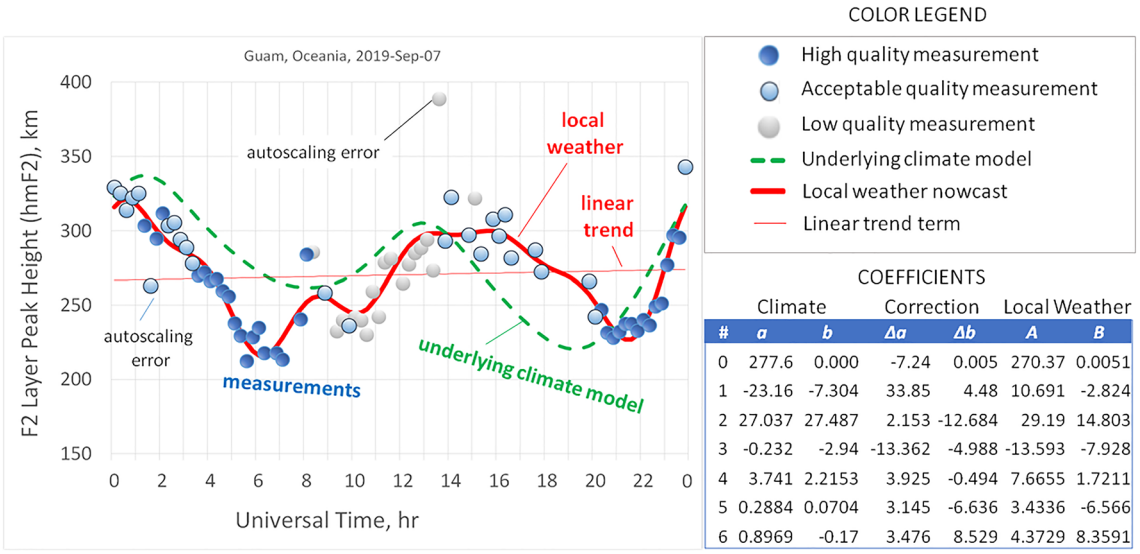

COEFFICIENTS

	Climate		Correction		Local Weather	
#	*a*	*b*	*Δa*	*Δb*	*A*	*B*
0	277.6	0.000	-7.24	0.005	270.37	0.0051
1	-23.16	-7.304	33.85	4.48	10.691	-2.824
2	27.037	27.487	2.153	-12.684	29.19	14.803
3	-0.232	-2.94	-13.362	-4.988	-13.593	-7.928
4	3.741	2.2153	3.925	-0.494	7.6655	1.7211
5	0.2884	0.0704	3.145	-6.636	3.4336	-6.566
6	0.8969	-0.17	3.476	8.529	4.3729	8.3591

Figure 2. Single-site assimilation of time-domain data. Differences between observed values (blue, light-blue, and gray circles) and the underlying model (green dashed line) are used to compute correction coefficients Δa and Δb that are then applied to the original model coefficients a and b to obtain the updated local weather model specification A and B (red solid line).

climate" applications where the temporal analysis method must avoid contributions from the underlying slow variability, for example, Wu et al. (2007). Once the coefficients Δa_i and Δb_i for $t = t_v$ are computed, it is technically possible to use Equation 4 for "forecasting" $V(t)$ for $t > t_v$, ever so limited in its span (see section 5.3).

The single-site expansion computations are illustrated in Figure 2, where time series of observed V_{obs} (blue, light-blue, and gray circles) and model V_{mod} (green dashed line) values are processed to derive Δa_i and Δb_i. Different color shades for the measured values V_{obs} in Figure 2 correspond to different quality scores of the measurement data that in this particular example are determined from the ARTIST Autoscaling Confidence Level (ACL) (Galkin et al., 2008, 2013; Galkin & Reinisch, 2008), an automatically determined metric produced by the intelligent system algorithm ARTIST as it extracts the value from the original remote sensing image. The ACL score is initialized to 100 in the beginning of the interpretation process and decreased each time ARTIST finds its computation or categorization to fail a quality check. The resulting 0–100 score range is split in five equal bands to characterize the outcome; two lower categories are excluded from assimilation. In addition to ACL, measurement *uncertainty bounds* are important for the data-driven modeling, as evident from recent next-generation research initiatives for Space Weather with Quantified Uncertainties (SWQU) at NSF (2019). Autoscaling uncertainty proved to be a function of ACL, severity of plasma disturbance, and station location (Galkin et al., 2013). We further address the data noise problem below in section 4.3. For testing and illustrative purposes, Figure 2 also plots the single-site (local) weather timeline V_{up} (red line) restored from the new set of coefficients $A_i = a_i + \Delta a_i$ and $B_i = b_i + \Delta b_i$ where a_i and b_i are the original coefficients of the climate model:

$$V_{up}(t) = A_0 + B_0 t + \sum_{i=1}^{H} A_i \cos iT + B_i \sin iT \quad (5)$$

4.3. Single-Site Expansion and Data Noise

If the available sensor instruments were capable of providing continuous error-free data acquisition and processing, the computation of Δa_i and Δb_i would present no difficulty. In practice, however, this is rarely the case. Gaps and erroneous values are common with many types of remote sensing equipment that require post-analysis for derivation of the actionable data. Ionosondes, the high frequency radio imagers of ionospheric plasma (e.g., Davies, 1990), are well known for the errors in data interpretation (Galkin et al., 2013; McNamara, 2006) that can propagate to the next stages of assimilative modeling unless conditioned. Conditioning of the data prior their assimilation is critically important, especially in 3DDA Kalman filter

schemas prone to data outliers. As seen in Figure 2, the NECTAR update operation suppresses occasional blunders of the intelligent system analysis and data jitter resulting from interference in the data acquisition and processing pipeline. This protection is one of the strong benefits of using the 4DDA scheme with its large time window of prior data. Failure to protect the assimilation in this manner had been found responsible for severe problems in transitioning the autoscaled-data-driven models to operations.

It is difficult to evaluate an instantaneous uncertainty of the ionogram-derived values, given that they are produced by an intelligent system prone to unknown, non-Gaussian errors of automatic ionogram interpretation. Instead, we treated the measurement uncertainty statistically so as to guide selection of the optimal diurnal expansion order, using an extensive study by Jones and Gallet (1962) who inspected diurnal spectra of a large multi-year set of manually scaled ionograms acquired from the 100+ site network established for the IGY campaigns of 1957–1958. Their study ruled out the diurnal harmonics above 8 as unrepresentative of the true physical variation. Using this result as the baseline, our decision was to retain the order to six harmonics, thus making the weather specification compatible with the formulation of climate representation in Equation 1.

Nominally, the single-site expansion in the time domain does not require interpolation, unless data collection is interrupted due to an instrument malfunction or anomalous geospace behavior. If temporal continuity of the sensor data flow cannot be guaranteed and data gaps in time are inevitable, the diurnal expansion of $\Delta V(t)$ becomes a case of unevenly spaced data series with the potential for the expansion solution to oscillate across some of the wider data gaps. To prevent these oscillations from entering subsequent stages of assimilation, missing data points are therefore filled with interpolated values prior to their expansion to constrain the analysis. In case of severe data losses, for example, for half a day, the interpolation algorithm slowly reduces the last observed ΔV_i to zero until observations resume. Given the importance of the first ΔV_i value after a wide gap, its ACL quality flag is analyzed and interpolation start may be postponed until sensor operations become confident. Naturally, nowcast quality in these extreme situations is not as good as the quality of backcast.

The same interpolation procedure replaces those ΔV_i values that are obtained using low-confidence observations V_{obs} (if the sensor instrument provides quality flags for its data). Even stronger concern of physically unreasonable representation of geosystems over the regions of missing data applies to the spatial domain.

4.4. Spatial Interpolation and Extrapolation of Diurnal Harmonics

Unconstrained spatial expansion in sparse and unevenly distributed sensor networks is likely to lead to unreasonable oscillations and runaway values of the fitting solution over regions with no sensors. Because NECTAR assimilation is arranged in terms of the observation/model *deviation*, a simple solution of constraining the spatial expansion would be to gradually reduce deviations to zero as they are extended from individual sensor locations to the global scale, thus returning to the underlying quiet-time specification over areas of missing data.

Particular choice of the spatial extrapolation technique is of a lesser importance; a suite of numerical algorithms for gap filling on a 2-D grid is readily available, ranging from the variety of 2-D splines (Wahba, 1990) and Kriging to the Tikhonov regularization method (Fridman et al., 2009). Because the gap filling is followed by another round of spatial expansion as discussed in section 4.5, the conventional gap filling methods that seek a smooth fit to a specific underlying function (such as Lagrange polynomial on a sphere) are less compelling for our task: they effectively double the assumptions about the solution formalism. Instead, we recommend the *2-D cellular automata* class of interpolators (Naumov, 2000) that evaluate summary facilitation of neighboring cells on the grid to compute the missing value. Once believed to be a powerful alternative to Kriging, the iterative cellular automata algorithms had not gained enough interest to become a standard offering in the statistical analysis packages. However, their capability to handle significantly irregular data grids becomes instrumental in space weather applications where sensor data coverage is relatively sparse, especially when acquired by unevenly distributed ground observatories. Additional motivation and justification for the iterative cellular automata schemes are given by Pariente and Laurini (1993) and Pariente (1994). Our particular preference in this class of interpolators is an algorithm that combines cellular automata computation with recurrent neural dynamics of the Hopfield feed-back neural network (Galkin et al., 2012; Hopfield, 1982).

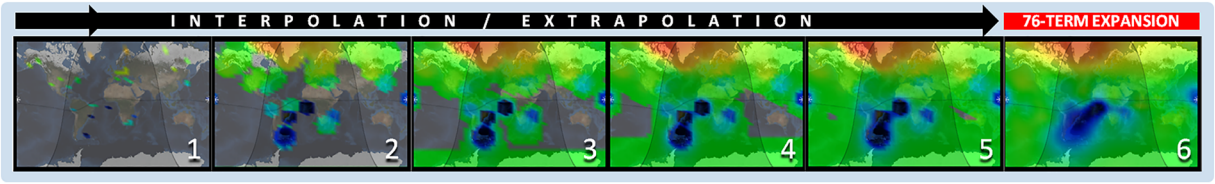

Figure 3. Successive steps of NECTAR processing of Δa_0 in the spatial domain. Frames 1–5: gap filling performed by cellular-automata class algorithm based on Hopfield recurrent neural network computation. Frame 6: Expansion into Jones-Gallet geographic function basis G_k represents the 2-D global map with 76 coefficients.

The neuron doctrine prescribes each neuron (one node of the map grid) to formulate its state as a weighted sum of facilitations from its neighboring neurons. This principle helps to avoid artificial gradients of NECTAR interpolation because each node of the grid considers its local context in all directions. Our interpolating Hopfield neural network is different from the conventional feed-forward back-propagation-trained perceptron architectures in that its weights are *not trained* on particular previous examples of interpolation. The weights are instead specifically formulated by the scientist to define the optimal outcome of the network as is evolves to its stable state. In our case, we (1) impose a correlation scale ellipse on the neuron facilitations that attenuates contributions from the grid nodes that are further away and (2) strengthen contributions from the nodes placed at the sensor sites. With the synaptic weights designed to these criteria, the neural network becomes a multiscale interpolator that preserves even minor features of the available observations while slowly and smoothly fading outside the sensor nodes. Finally, the Hopfield dynamics is placed under the simulated annealing protocol that enhances its restorative capability as the network "tunnels" through its local minima of the energy function to approximate the desired global optimization. Further detail of the NECTAR synaptic weight engineering and dynamics is beyond the scope of this introductory description, to be presented in our subsequent publications on the topic, along with the evidence of its performance.

An example interpolation sequence is shown in Figure 3, where the leftmost frame 1 corresponds to the starting point of the processing (data from 56 GIRO locations) and frames 2–5 illustrate the algorithm progression.

4.5. Spatial Expansion in Jones-Gallet Geographic Basis G_k

Once the spatial interpolation for the diurnal coefficients Δa_i and Δb_i has been performed, each grid is spatially expanded into the Jones-Gallet basis of geographic functions $G_k(\lambda_G, \phi_G)$ to complete the update step of assimilation. The spatial expansion algorithm starts with orthonormalization of the original basis $G_k(\lambda_G, \phi_G)$ to an interim basis $F_k(\lambda_G, \phi_G)$ (Jones & Gallet, 1962). The interim coefficients m_k are obtained by a least squares fit (LSF) to the gap-filled 2-D grid of the differences (computed by interpolation-extrapolation process explained above in section 4.4). Ordinary least-squares computation with 76 unknowns to the grid is unrealistic, so an iterative approximate procedure applies a single-term LSF to the current residual in many finite small steps. This procedure does not account for the original uncertainty/confidence attribute of the nodes, and neither it places higher weights on the sensor-populated areas of the grid. The resulting fit therefore tends to oversmooth data features and undercompensate the climate-measurement differences over the sensor sites, which will be addressed in our future work. Finally, the computed interim coefficients m_k are inverted back into the original basis $G_k(\lambda_G, \phi_G)$ to obtain the resulting c_k solution. The rightmost frame in Figure 3 illustrates the outcome of expansion to the Jones-Gallet basis.

The expansion of each diurnal harmonic Δa_i and Δb_i is done successively, and the resulting set of correcting coefficients Δc_{ij} is simply added to the underlying quiet-time model coefficients c_{ij} to form the updated model specification. This updated coefficient set provides the global 2-D specifications of $V(t)$ for $t_v - 24\ \text{hr} < t < t_v$.

5. Spatial and Temporal Predictive Capabilities of NECTAR

Testing of the NECTAR algorithm was done using the IRI-based Real-Time Assimilative Model (IRTAM) (Galkin et al., 2012) of the F2 region peak ionospheric plasma density N_mF2, or the corresponding plasma frequency f_oF2. For comparisons with background climatology, IRI maps of f_oF2 were selected (ITU-R, 2009), driven by the definitive (rather than predicted) ionospheric index of the solar activity, IG12

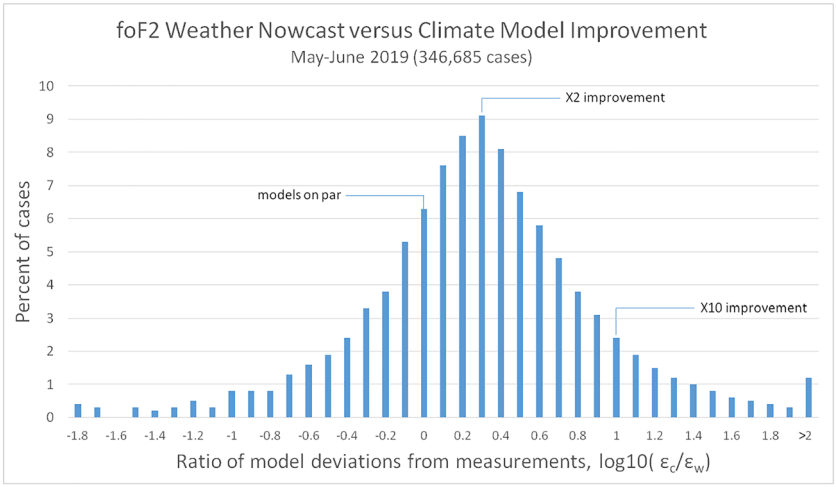

Figure 4. Probability distribution of the f_oF2 climate/weather model deviation ratio in the logarithmic scale, $\log_{10}(R_{cw})$, describing improvement of the weather versus climate specification.

(Liu et al., 1983), acquired from the Empirical-Canadian High Arctic Ionospheric Model (ECHAIM) supplementary support software site at https://chain-new.chain-project.net/index.php/chaim/e-chaim/supplementary-support-software. The model comparisons were conducted by (1) establishing the baseline model performance at all contributing GIRO locations and then (2) analyzing losses of the established baseline in spatial and temporal prediction regimes. To evaluate the performance, model versus measurement deviations were computed as $\varepsilon_c = V_{climate} - V_{observed}$ and $\varepsilon_w = V_{weather} - V_{observed}$, and various statistical quality metrics were then built based on the deviation ratio $R_{cw} = |\varepsilon_c/\varepsilon_w|$.

Overall, the statistical analysis of the IRTAM performance shows that the R_{cw} deviation ratio complies with the log-normal rather than Gaussian distribution with significant tail sections, which is expected given our use of the absolute ratio value in R_{cw} definition. For illustration, Figure 4 shows a histogram of IRTAM nowcast ratios in the logarithmic scale, $\log_{10}(R_{cw})$, built using data from 59 GIRO stations during May–June 2019, totaling ~350,000 comparison cases. The distribution mode corresponds to ×2 improvement of IRTAM over the quiet-time climate specification.

Further testing results are described by first illustrating the *spatial* prediction capability of NECTAR on a particular case example, then presenting the control-site test statistics data, and finally, discussing temporal prediction capabilities of IRTAM.

5.1. Spatial Prediction: Case Study

Figure 5 presents the IRTAM map of f_oF2 for 17 October 2012 1830 UT obtained during a strong positive ionospheric weather event detected at American longitudes. The color surface maps display the IRTAM-calculated deviations from the IRI background model, while the colored dots depict the difference between observed and IRI value of f_oF2 at the GIRO site locations. The same color legend is used for both surface and dots, green color meaning: no difference.

The NECTAR calculation used for the map in Figure 5a did not include any GIRO observations from Africa, and it is unexpected to see the strong Δf_oF2 enhancement (red) stretch into West Africa. One would expect a gradual transition to zero (green) eastward of the GIRO sensor on Ascension Island (yellow dot). Inclusion of the South African GIRO observations in the NECTAR analysis (Figure 5b) reveals a moderate f_oF2 enhancement north of the South African GIRO sites. On the same map in Figure 5a, examples of this NECTAR feature can be seen; for example, positive deviation of f_oF2 observed at Port Stanley (P.S.) station in South America is not extended westward and instead tapers off to return to the background IRI. Moreover, analysis of observed Δf_oF2 at Fortaleza (FO) in Brazil and Ascension Island in the South Atlantic Ocean suggests that ΔfoF2 gradient would be naturally fading eastwards.

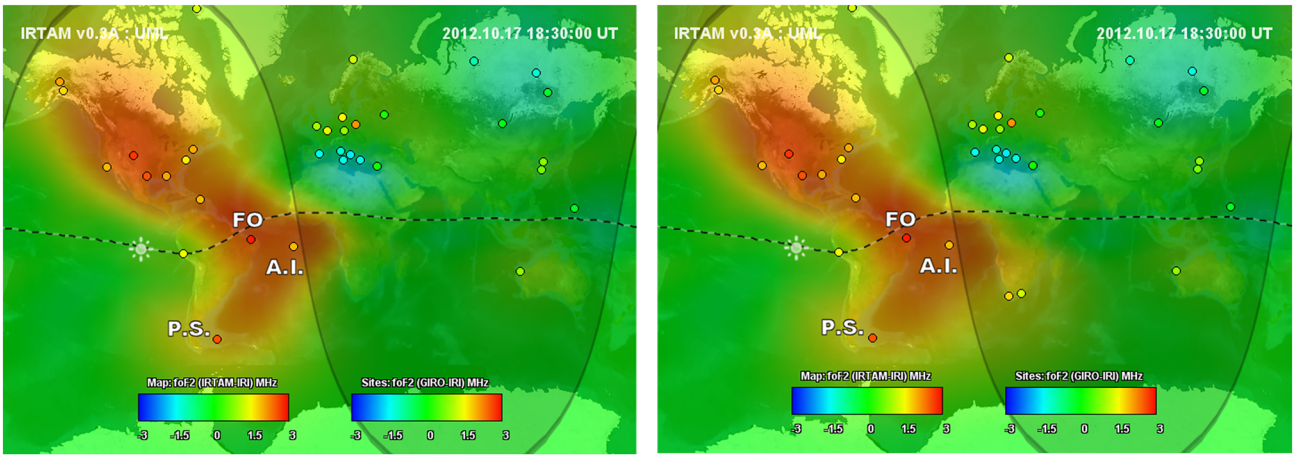

Figure 5. Map of NECTAR-computed f_oF2 deviation from its quiet-time IRI climatology for 17 October 2012 1830 UT. (a) Strong positive Δf_oF2 at American longitudes; surprisingly, this effect stretches into Western Africa although Ascension Island (A.I.) measurements (yellow dots) and the absence of any African measurements suggest diminishing impact of the ionospheric weather eastward of A.I. (b) Same map, but including measurements from the South African network support the NECTAR extrapolation analysis.

Closer inspection of the temporal harmonic maps reveals a significant positive 12-hr deviation harmonic effect over Ascension Island. This significant effect is then extrapolated by NECTAR over to reach the African coast (Figure 6a).

Combined with only minor changes in diurnal deviation detected over the South American sector, these findings explain why NECTAR suggests stronger effect eastward of the Fortaleza site in comparison with its westward counterpart from Ascension Island to Jicamarca. Figure 6b presents timelines for Ascension Island measured (dots) and modeled values (green dashed line for the background IRI and red solid line for the local weather computation) for the 24-hr period prior to the NECTAR computation time. Indeed, the (measurement-IRI model) f_oF2 deviation timeline (green line) shows a wave pattern with positive and negative phases of approximately 15-hr period (black dash-dotted line). The pattern is detected by the harmonic analysis as a strong 12-hr harmonic event that extrapolates with attenuation outward the observatory location and results in the West African enhancement in Figure 5a. To validate this outcome of the NECTAR computation, the same processing was repeated with assimilation of additional measurements from the South African sensor network (Figure 5b) to conclude that predictive analysis is quite reasonable, at least in this particular case. Further optimization of the extrapolation covariance is warranted in a follow-on investigation, based on similar test-case strategy and additional observations from independent sensors.

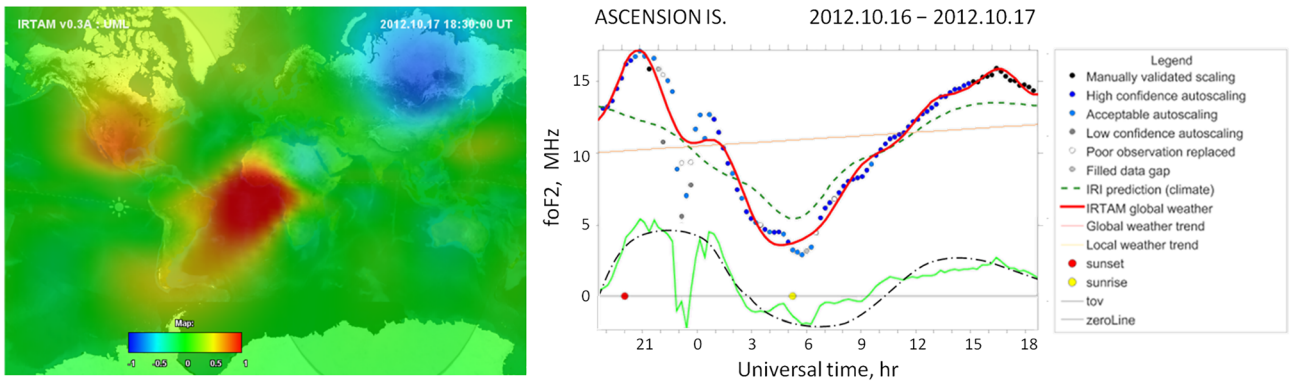

Figure 6. (a) Color-coded map of the 12-hr harmonic of the f_oF2 deviations calculated for t_v = 1830UT on 17 October 2012 shows strong enhancement over the Ascension Island GIRO sensor. (b) Timeline comparison of the measurements (dots) with the background IRI model (green dashed line) for Ascension Island. The measurement-IRI deviation timeline (green line) reveals a wave pattern with a ~15-hr period (black dash-dotted line), detected by NECTAR as the 12-hr harmonic.

Table 1
Control Site Testing of IRTAM-2012 Using North American Digisonde Sites

Station	Station ID	Improvement *F*, included	Improvement *F*, excluded	Quality loss
Boulder, CO	BC840	2.20	1.75	20%
Idaho Falls, ID	IF843	1.92	1.39	28%
Wallops Is., VA	WP937	2.14	1.46	32%
Austin, TX	AU930	2.10	1.34	36%
Eglin AFB, FL	EG931	2.00	1.28	36%
Millstone Hill, CA	MHJ45	2.11	1.24	41%
Point Arguello, CA	PA836	2.61	1.29	51%
Puerto Rico	PRJ18	2.86	1.05	63%

5.2. Spatial Prediction: Statistics

Quantitative evaluation of the spatial prediction capability of NECTAR was done statistically by characterizing IRTAM's capability to reproduce the ionosphere at control GIRO locations that were excluded from assimilation (Vesnin, 2014). A Loss of Quality (LQ) parameter was introduced for each GIRO site as a metric of IRTAM accuracy reduction if that location was excluded. LQ is defined using an "improvement factor" F as

$$\mathrm{LQ} = \frac{\mathrm{F_{included}} - \mathrm{F_{excluded}}}{\mathrm{F_{included}}} \cdot 100\%. \tag{6}$$

Improvement factors are defined (see below) as statistic measures to characterize the absolute ratio of climate over weather errors R_{cw}:

$$R_{\mathrm{cw}} = \left| \frac{\mathrm{V_{climate}} - \mathrm{V_{observed}}}{\mathrm{V_{weather}} - \mathrm{V_{observed}}} \right| = \left| \frac{\varepsilon_{\mathrm{c}}}{\varepsilon_{\mathrm{w}}} \right| \tag{7}$$

where ε_c and ε_w are deviations of models from the measurements. R_{cw} is equal to 1 when both climate and weather models are on par in terms of their accuracy and is greater than 1 when the weather model has a smaller error. Three versions of the *F* metric were used in our statistical analysis, each addressing various aspects of the IRTAM performance:

$$F_{\mathrm{M}} = \mathrm{median}\{R_{cw}\}_{\mathrm{i}=1..N} \tag{8}$$

$$F_{\mathrm{A}} = \frac{\sum_{\mathrm{i}=1}^{N} |\epsilon_{\mathrm{c}}|}{\sum_{\mathrm{i}=1}^{N} |\epsilon_{\mathrm{w}}|} \tag{9}$$

$$F_{\mathrm{S}} = \frac{\sum_{\mathrm{i}=1}^{N} \left(\frac{\max\{|\epsilon_{\mathrm{c}}|, \xi\}}{\max\{|\epsilon_{\mathrm{w}}|, \xi\}} \right)}{N} \tag{10}$$

where *N* is the number of GIRO sites and ξ is the measurement uncertainty due statistical data noise.

The median-based F_{M} definition excludes the extreme weather cases that climate models, by design, are not intended to represent. It is therefore best suited for evaluation of the normal day-to-day weather variability of the ionosphere with respect to the IRI reference specification of one typical quiet day.

The average-over-sites metric F_{A} gives a generic sense of central tendency with no regard to the model performances specific to individual locations. Unless the *N* locations are clustered by a suitable

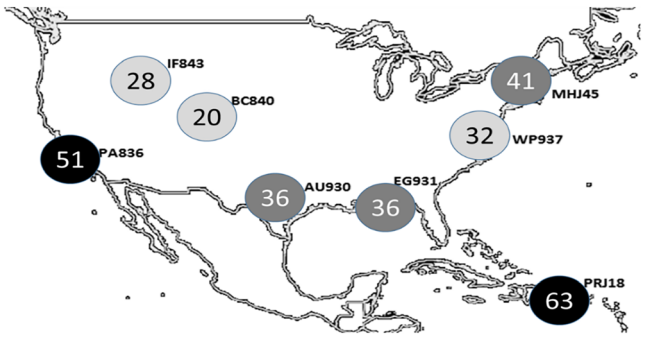

Figure 7. Control-site testing of NECTAR in the North American network of 8 Digisonde sounders (Reinisch et al., 2009). Circled values at site locations correspond to the Loss of Quality, LQ, when the site data are excluded from assimilation. Darker circles correspond to stations of higher importance to nowcast and less replaceable measurements.

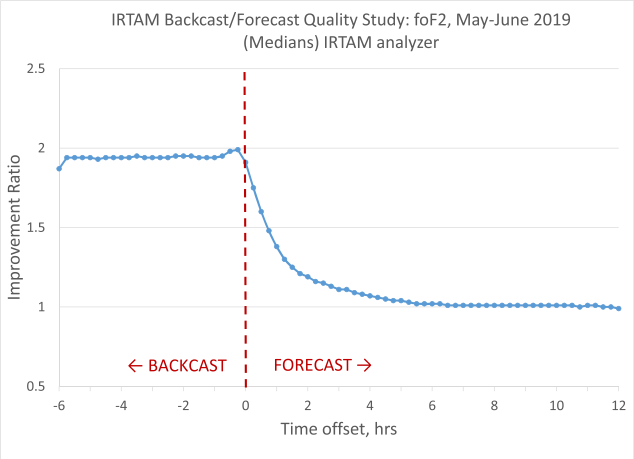

Figure 8. NECTAR improvement factor F as function of the backcast/nowcast/forecast time offset (statistical average for model computations in May–June 2019 using re-analysis of data from 60 GIRO stations and quiet-time statistic F_M).

attribute such as the geomagnetic latitude, F_A tends to represent the majority of the site population in the comparisons.

The average improvement metric F_S is strongly affected by the large individual R_{cw} values. As such, F_S highlights locations and times of large deviations of the ionospheric conditions from the quiet-time reference. Large site-specific R_{cw} values may also correspond to occasional cases of minute deviations of IRTAM from observations, ε_w. In order to diminish the influence of very small ε_w on the F_S analysis, computed deviations are compared to the uncertainty ξ of the ionosonde measurements to avoid falling below it.

All improvement factors were found varying significantly with the sensor latitude and level of solar and geospace activity. The greatest improvement is observed at low latitudes, especially in the equatorial ionization anomaly crests. A more modest improvement is observed at the mid-latitude locations during low solar activity where IRI tends to be more accurate in its description of the quiet conditions. A detailed analysis of F_A variability, with clusterization of comparison data by location of GIRO sites, data quality, local time, level of solar activity, and geospace disturbance indicators, was conducted by Vesnin (2014), suggesting that improvement of the weather modeling is higher during disturbed periods of time and for low and high latitude locations, fairing on average at 2.0 improvement factor for all tested data.

The LQ metric based on F_A computation varies significantly across various sensor locations as well. An example statistical study that involved GIRO stations in North America (Table 1, Figure 7) (Vesnin, 2014) for the period from February to June 2013 yielded LQ values ranging from 20% to 63% (values inside the circles in Figure 7).

At the locations where the quality loss metric LQ is smaller, IRTAM is able to more accurately restore the excluded measurements from data from neighboring sensor sites. All of such low-LQ nodes are internal within the network. The external and remote observatory sites such as Millstone Hill or Puerto Rico are more important to the weather model performance. In fact, $F_{excluded}$ at the Puerto Rico site PRJ18 is 1.05, which means that the weather specification without assimilation of PRJ18 data is essentially no more accurate than the background climate model at that location at the edge of the Appleton anomaly crest where specific effects, such as pre-reversal enhancements, cannot be simply extrapolated from neighboring stations outside of the region.

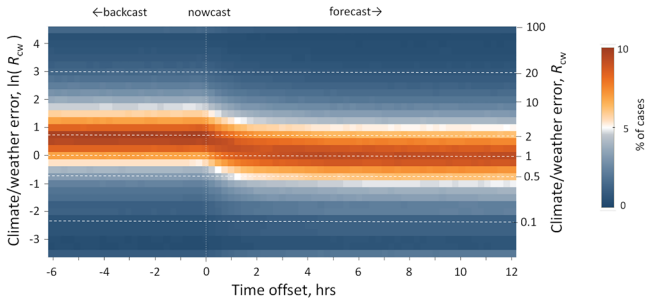

Figure 9. Distribution histograms of R_{cw}, climate versus weather deviation of model from GIRO measurements, computed for time offsets from −6 (backcast) to 12 (forecast) hours. Individual histograms are computed for each time offset and placed vertically along the horizontal axis with color corresponding to % of cases. Each histogram is computed from a 346,685 case sample of R_{cw} values in May–June 2019.

5.3. Temporal Prediction

Predictive properties of NECTAR in the time domain were studied using retrospective GIRO data collections in so-called "re-analysis" mode of IRTAM computations. As in the real-time mode, the reanalyzing IRTAM derives its specification using 24-hr deviation histories up to t_v, only that now it is possible to access measurements past t_v for evaluation of the model in its forecast regime. Thus obtained NECTAR representation of the 24-hr data prior to t_v is advanced into "future" and compared to "future" measurements. Intuitively, the improvement factors F should drop once the model enters its forecast regime and then should continue diminishing as the forecast advances further into the future.

5.3.1. Quiet-Time Performance

Evaluation of IRTAM performance during quiet time is conducted using the median-based F_M metric for time offsets from −6 to +12 hr. For each of the 73 offsets, F_M values are obtained over 5,860 IRTAM computation instances using data from 59 GIRO observatories operating during May–June 2019. As seen in Figure 8,

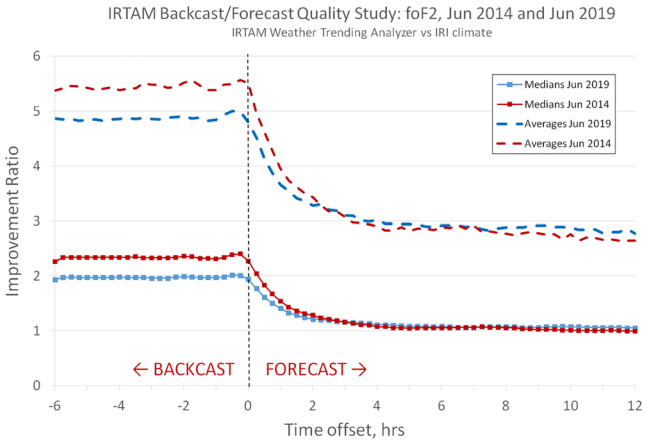

Figure 10. NECTAR model performance for periods of high and low solar activity using median F_M and average F_S metrics.

quality of the IRTAM description is consistent over different backcast offsets, with about ×2 improvement versus the IRI climate specification, in good agreement with results obtained using all-locations F_A metric.

In the forecast regime $t > t_v$, IRTAM gradually returns to the background IRI for increasing forecast time offsets. This confirms the intended purpose of the F_M metric to narrow the evaluation down to the quiet-time weather variability: once no prompt measurements are available for assimilation, IRTAM becomes increasingly consistent with the monthly average climate specification. Remarkably, forecast quality undergoes a rapid decline by ~75% beyond only 2 hr from t_v.

5.3.2. R_{cw} Probability Distribution in Backcast/Forecast Mode

Figure 9 presents histograms of R_{cw} ratios of model deviations (as shown in Figure 8) computed for the backcast-to-forecast time offsets of −6 to +12 hr and vertically stacked with the color scale mapped to the percentage of counts in the histogram. Total number of model comparisons performed for this analysis is (2 months at 15-min cadence) × 59 GIRO stations × 73 time offsets ~25 million cases.

Dependency of the R_{cw} distribution mode (i.e., the most probable value) on the time offset is in a good agreement with analysis of the median-based F_M factor, which confirms its similar independence on the outliers: $P_{max}(R_{cw})$ remains fairly constant at ~2.1 for all backcast and nowcast times, falling rapidly within 1–2 hr in the forecast regime to the background climate model. Although no other outstanding features are visible in this example computation, additional statistical considerations can be drawn for the temporal prediction performance of IRTAM from analysis of the distribution extremes above 1.

5.3.3. IRTAM Performance in Non-Quiet Conditions

In order to evaluate IRTAM descriptions of the ionospheric weather far from the quiet-time IRI expectations, the climate/weather error ratios R_{cw} have to be statistically inspected in their upper tail section of the probability distribution $P(R_{cw})$. "Non-quiet" conditions are defined by their deviations from the quiet-time ionosphere timeline with no regard to the processes that cause these major deviations, no matter of their origin. One simple way of sensing the tail section of $P(R_{cw})$ contributions is to compute the average of R_{cw} over GIRO locations F_S from Equation 10, instead of its median F_M, because the F_S metric is sensitive to contributions from larger improvement ratios observed at certain GIRO sites.

Figure 10 presents comparisons of the F_M and F_S computations for two different summer periods: low solar activity in June 2019 and high solar activity in June 2014.

Both median-based F_M and average-based F_S charts reveal similar features in IRTAM/IRI performance: In the nowcast and backcast regimes, IRTAM demonstrated about 10% higher improvement during more active Sun and a rapid return to the same background level in the forecast regime. In the forecast regime, however, the site-specific F_S metric demonstrates that IRTAM is able to retain the data assimilation benefits at certain sensor locations, instead of simply reducing back to the IRI climatology. In support of this conclusion, we studied one particular type of the ionospheric phenomena that eludes characterization in the climate models, so-called post-sunset uplift of the equatorial F region, whose progression resists reliable description in terms of the average climatology (e.g., Adeniyi et al., 2003). To illustrate the effect and its duration, IRTAM and IRI errors ε_c and ε_w for the peak height of F2 layer h_mF2 are shown in Figure 11 for one equatorial station in Jicamarca, Peru, averaged over 2003–2014 period but sorted by the offset relative to the local sunset time. Clearly, IRTAM has advantage in representing this significantly weather-driven phenomenon for about 10 hr since the sunset.

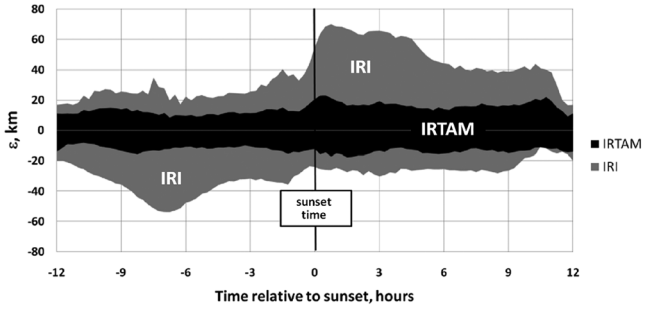

Figure 11. Dependence of climate and weather deviations, ε_w and ε_c, of the F2 layer peak height h_mF2, on the offset from local sunset time at equatorial locations. Deviations are sorted by the time offset from the sunset before averaging, using measurements acquired in 2003–2014 in Jicamarca, Peru.

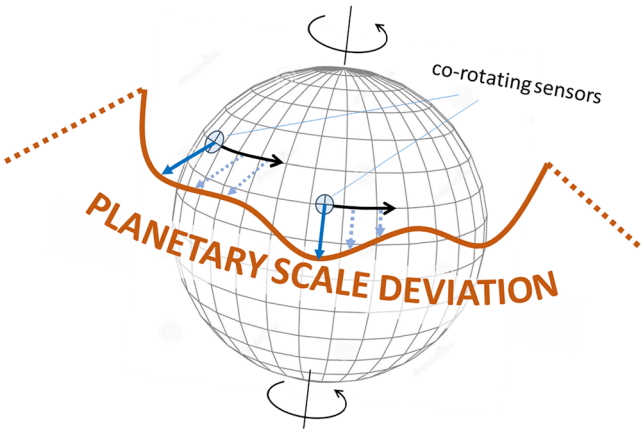

Figure 12. Spatial planetary scale deviation, static in the Sun-Earth frame (brown line), is observed by the ground sensors (crossed circles) in time as they co-rotate with the Earth. When GAMBIT extrapolates the diurnal deviation harmonics spatially, lower orders of the temporal expansion have large covariance along the co-rotation trajectory.

Analysis of the storm-time IRTAM performance beyond the relatively stable summer periods of 2014 and 2019 can be found in Vesnin (2014) and will remain an active research topic.

6. Diversity of Input Data Sources

In summary, NECTAR model morphing is based on three general principles: (1) Weather nowcast uses a well-established climatology model as the starting point of assimilation, (2) the climatology specifications are smoothly and iteratively morphed to match the 24-hr history of observed measurement-versus-climate deviations at the sensor sites, and (3) the morphing procedure detects diurnal harmonics of ongoing weather processes that, because these persist for hours, are assumed to accordingly extend in space. Although wave processes are ubiquitous in space, responsible for the energy transfers, the weather phenomena do not to necessarily exhibit a wave nature, in which case NECTAR will not be able to detect their manifestation in the diurnal harmonics to restore missing observations. However, it will detect and represent the phenomenon itself in the measurement data. Therefore, while NECTAR principles are not universally applicable to all domain of the Sun-driven space weather, much less the geophysics as a whole, NECTAR-based models can assimilate a variety of real-time data sources in multiple disciplines. In our particular example of IRTAM, the model morphing procedure can accommodate the multitude of ongoing research to overcome the scarceness of ionospheric measurements (e.g., Scherliess et al., 2009; Fridman et al., 2009, 2016; Froń et al., 2018; and many others) by involving new and emerging types of sensor instrumentation.

7. Discussion and Summary

The NECTAR technique of assimilative modeling views geosystems in terms of their internal periodic constituents, which strengthens the restorative capability at the assimilation update step, specifically when only a limited number of observatories is available for the weather nowcast. When applied to sparse spatial data, NECTAR acts as an associative nonlinear multiscale interpolator of missing information. Simply put, it detects the observed periodic deviations of measurements from the climatology at observatory locations and extends them spatially away from the site because they are found persisting in time and therefore in space. Early tests of the NECTAR morphing reveal its enhanced capability to predict system dynamics over no-data regions (spatial interpolation), though little improvement in short-term forecast.

In the spatial domain, testing of NECTAR principles using the GIRO network of sensors suggests that missing dynamic features of the ionosphere can be gleaned using data from neighboring locations, though with varying degree of success. Indeed, space weather variability may include periodic components that reflect greater (planetary) scale processes that develop in the Sun-Earth reference frame. The co-rotating remote sensing observatories are able to detect such slow planetary-scale variability component, continuously in time. Figure 12 illustrates the concept by showing a planetary-scale static deviation component in space (brown line) that observatories (two circles) sense in time as they corotate with the Earth. The lower expansion orders in the diurnal deviation basis harmonics, once considered spatially, can therefore correlate over large distances in the zonal direction along the corotation path, thus enhancing the spatial prediction properties of NECTAR. Naturally, detected harmonic deviations cannot be universally projected everywhere else. If they are projected too far beyond the spatial scale of their harmonic wave pattern, the artificial horizontal gradients would arise to disturb the HF communications modeling. Gradual return to the undisturbed background definition over distance is a safer approach. Fine-tuning the correlation ellipses will be one of the important topics for future IRTAM research.

In the temporal domain, NECTAR tests suggest that, without any consideration of the geospace activity state, overall quality of the weather description falls back to the background climatology within only

1–2 hr. Such minute improvement to the well-established short "memory span" of the ionosphere is somewhat disappointing, suggesting that acquired sensor measurements of even 1-hr delay in arrival to the data processing facility are actually already too old, providing only minor contribution to the weather service. Only in certain particular scenarios that do resist climatologic description, such as the post-sunset dynamics of the equatorial ionosphere, the assimilative weather model can retain some of its advantages in the forecast regime. Needless to say, the linear trend term over previous 24 hr of ionosphere life does not work too well in the forecast mode beyond a few hours. Further improvement of the temporal predictive properties of the assimilative empirical models of the ionosphere will require special effort to capture timelines of its behavior in the context of the geospace activity, similar to the effort of Araujo-Pradere et al. (2002) to build a storm-time extension of IRI.

Data Availability Statement

Digisonde data have been provided via agreement between the U.S. Air Force 557th Weather Wing and the Digital Ionogram DataBase (DIDBase, http://ulcar.uml.edu/DIDBase) of Global Ionosphere Radio Observatory (GIRO), http://spase.info/SMWG/Observatory/GIRO, homepage at http://giro.uml.edu. Ascension and Guam Island ionosonde data are acquired from the U.S. Air Force NEXION Digisonde network (Mark Leahy, program manager). Data from the Fortaleza station are made available to GIRO through the EMBRACE program from the National Institute for Space Research (INPE, Inez Batista), Brazil. The Port Stanley ionosonde is operated by the Rutherford Appleton Laboratory (Ruth Bamford), UK. The homepage of the IRI project is at http://irimodel.org and for IRTAM at http://giro.uml.edu/IRTAM/. Records of the IG12 activity index were downloaded from ECHAIM portal at https://chain-new.chain-project.net.

Open Research

Access to IRI and IRTAM model computations is free for academic purpose at Global Assimilative Model of Bottomside Ionosphere Timeline (GAMBIT) public data repository of GIRO at http://giro.uml.edu/GAMBIT via GAMBIT Explorer software.

Acknowledgments

I. G. and B. R. were in part supported by IARPA under AF contract #A865016C9104 to SWRI/LDI/UML.

References

Adeniyi, J. O., Bilitza, D., Radicella, S. M., & Willoughby, A. A. (2003). Equatorial F2-peak parameters in the IRI model. *Advances in Space Research*, *31*(3), 507–512. https://doi.org/10.1016/S0273-1177(03)00039-5

Araujo-Pradere, E., Fuller-Rowell, T., & Codrescu, M. (2002). STORM: An empirical storm-time ionospheric correction model, 1. Model description. *Radio Science*, *37*(5), 3-1–3-12. https://doi.org/10.1029/2001RS002467

Bilitza, D. (Ed) (1990). *International Reference Ionosphere 1990*, *Report NSSDC/WDC-A-R&S 90-22* (p. 155). Greenbelt, Maryland: National Space Science Data Center.

Bilitza, D., Altadill, D., Truhlik, V., Shubin, V., Galkin, I. A., Reinisch, B. W., & Huang, X. (2017). International Reference Ionosphere 2016: From ionospheric climate to real-time weather predictions. *Space Weather*, *15*, 418–429. https://doi.org/10.1002/2016SW001593

Davies, K. (1990). *Ionospheric radio*, *IEE Electromagnetic Waves Series 31*. London: Peter Peregrinus Ltd.

Fridman, S. V., Nickisch, L. J., Hausman, M., & Zunich, G. (2016). Assimilative model for ionospheric dynamics employing delay, Doppler, and direction of arrival measurements from multiple HF channels. *Radio Science*, *51*(3), 176–183. https://doi.org/10.1002/2015RS005890

Fridman, S. V., Nickisch, L. J., & Hausman, M. A. (2009). Personal-computer-based system for real time reconstruction of the three-dimensional ionosphere using data from diverse sources. *Radio Science*, *44*, RS3008. https://doi.org/10.1029/2008RS004040

Froń, A., Galkin, I. A., Krankowski, A., Hernandez-Pajares, M., Bilitza, D., Reinisch, B. W., et al. (2018). Real-time mapping of VTEC and slab thickness in cooperation of IGS' GNSS and GIRO sensor networks. In *Proc. 2018 2nd URSI Atlantic Radio Science Meeting (AT-RASC)*. Ghent, Belgium: International Radio Science Union. https://doi.org/10.23919/URSI-AT-RASC.2018.8471384

Galkin, I. A., Khmyrov, G. M., Kozlov, A. V., Reinisch, B. W., Huang, X., & Paznukhov, V. V. (2008). The ARTIST 5, in Radio Sounding and Plasma Physics. In *AIP Conf. Proc.*, *974*(1), 150–159. https://doi.org/10.1063/1.2885024

Galkin, I. A., & Reinisch, B. W. (2008). *The new ARTIST 5 for all digisondes*, *Ionosonde Network Advisory Group (INAG) Bulletin* (No. 69 ed.). Ghent, Belgium: International Radio Science Union. Retrieved from http://www.ursi.org/files/CommissionWebsites/INAG/web-69/2008/artist5-inag.pdf

Galkin, I. A., Reinisch, B. W., Huang, X., & Bilitza, D. (2012). Assimilation of GIRO Data into a Real-Time IRI. *Radio Science*, *47*. https://doi.org/10.1029/2011RS004952

Galkin, I. A., Reinisch, B. W., Huang, X., & Khmyrov, G. M. (2013). *Confidence score of ARTIST-5 ionogram autoscaling*, *Ionosonde Network Advisory Group (INAG) Bulletin* (No. 73 ed.). Ghent, Belgium: International Radio Science Union. Retrieved from http://www.ursi.org/files/CommissionWebsites/INAG/web-73/confidence_score.pdf

Gauthier, P., Tanguay, M., Laroche, S., Pellerin, S., & Morneau, J. (2007). Extension of 3DVAR to 4DVAR: Implementation of 4DVAR at the Meteorological Service of Canada. *Monthly Weather Review*, *135*(6), 2339–2354. https://doi.org/10.1175/MWR3394.1

Ghil, M., Cohn, S., Tavantzis, J., Bube, K., & Isaacson, E. (1981). Applications of estimation theory to numerical weather prediction. In A. L. Bengtsson, M. Ghil, & E. Kallen (Eds.), *Dynamic meteorology: Data assimilation methods* (pp. 139–224). New York: Springer-Verlag.

Hopfield, J. J. (1982). Neural networks and physical systems with emergent collective computational abilities. *Proceedings. National Academy of Sciences. United States of America*, *79*(8), 2554–2558. https://doi.org/10.1073/pnas.79.8.2554

International Telecommunications Union - Radiocommunication (2009). *ITU-R reference ionospheric characteristics*. Geneva: International Telecommunication Union. Recommendation P.1239–2 (10/2009). Retrieved from http://www.itu.int/rec/R-REC-P.1239/en

Jones, W., & Gallet, R. (1962). Representation of diurnal and geographic variations of Ionospheric data by numerical methods. *Journal Research*, *66D*(4), 419–438.

Jones, W., Graham, R. P., & Leftin, M. (1969). *Advances in ionospheric mapping by numeric methods, ESSA Technical Report ERL 107-ITS 75*. Boulder, CO: U.S. Dept. commerce, ESSA.

Liu, R., Smith, P., & King, J. (1983). A new solar index which leads to improved f_oF2 predictions using the CCIR atlas. *Telecommunication Journal*, *50*(8), 408–414.

Lorenc, A. C. (1986). Analysis methods for numerical weather prediction. *Quarterly Journal of the Royal Meteorological Society*, *112*(474), 1177–1194. https://doi.org/10.1002/qj.49711247414

McNamara, L. F. (2006). Quality figures and error bars for autoscaled Digisonde vertical incidence ionograms. *Radio Science*, *41*, RS4011. https://doi.org/10.1029/2005RS003440

McNamara, L. F., Baker, C. R., & Decker, D. T. (2008). Accuracy of USU-GAIM specifications of f_oF2 and M(3000)F2 for a worldwide distribution of ionosonde locations. *Radio Science*, *43*. https://doi.org/10.1029/2007RS003754

Mitchell, T. M. (1980). *The need for biases in learning generalizations, Rutgers Tech.Rep. CBM-TR 117*. New Brunswick, New Jersey, USA: Rutgers University. https://citeseerx.ist.psu.edu/viewdoc/summary?doi=10.1.1.19.5466

Naumov, A. Y. (2000). Design of GIS data types for environmental modeling: Using the concept of field data type for dealing with spatial continuity. In *4th International Conference on Integrating GIS and Environmental Modeling: Problems, Prospects and Research Needs* (pp. 1–12). Banff, Alberta, Canada: GIS/EM4.

NSF (2019). *Next generation software for data-driven models of SpaceWeather with quantified uncertainties (SWQU), Program Solicitation NSF 20-519*. Alexandria, Virginia: National Science Foundation. Retrieved from https://www.nsf.gov/pubs/2020/nsf20519/nsf20519.pdf

Pariente, D. (1994). Geographic interpolation and extrapolation by means of neural networks. In *Proc. Fifth European Conference and Exhibition on Geographical Information Systems (EGIS/MARI'94)* (Vol. 1, pp. 684–693). Utrecht/Amsterdam: EGIS Foundation.

Pariente, D., & Laurini, R. (1993). Statistical spatio-temporal data interpolation and extrapolation based on neural networks. In *Proc. Workshop on New Tools for Spatial Analysis*, Nov 18-20, 1993 (pp. 92–101). Lisbon, Portugal: DOSES/EUROSTAT.

Rani, M., Dhok, S. B., & Deshmukh, R. B. (2018). A Systematic Review of Compressive Sensing: Concepts, Implementations and Applications. *IEEE Access*, *6*, 4875–4894. https://doi.org/10.1109/access.2018.2793851

Rawer, K. (1963). Propagation of decameter waves (HF band). In B. Landmark (Ed.), *Meteorological and astronomical influences on radio wave propagation* (pp. 221–250). New York: MacMillian Company.

Reinisch, B. W., & Galkin, I. A. (2011). Global ionospheric radio observatory (GIRO). *Earth and Planetary Science*, *63*(4), 377–381. https://doi.org/10.5047/eps.2011.03.001

Reinisch, B. W., Galkin, I. A., Khmyrov, G. M., Kozlov, A. V., Bibl, K., Lisysyan, I. A., et al. (2009). The New Digisonde for Research and Monitoring Applications. *Radio Science*, *44*, RS0A24. https://doi.org/10.1029/2008RS004115

Reithinger, F., Jank, W., Tutzy, G., & Shmueli, G. (2008). Modeling price paths in on-line auctions: Smoothing sparse and unevenly sampled curves by using semiparametric mixed models. *Journal of the Royal Statistical Society: Series C*, *57*(2), 127–148. https://doi.org/10.1111/j.1467-9876.2007.00605.x

Rice, J. R. (1993). *Numerical methods in software and analysis*. Academic Press. https://doi.org/10.1016/B978-0-12-587755-8.50002-1

Rush, C., Fox, M., Bilitza, D., Davies, K., McNamara, L. F., Stewart, F., & PoKempner, M. (1989). Ionospheric mapping—An update of f_oF2 coefficients. *Telecommunication Journal*, *56*, 179–182.

Scherliess, L., Thompson, D. C., & Schunk, R. W. (2009). Ionospheric dynamics and drivers obtained from a physics-based data assimilation model. *Radio Science*, *44*. https://doi.org/10.1029/2008RS004068

Schunk, R. W., Scherliess, L., Eccles, V., Gardner, L. C., Sojka, J. J., Zhu, L., et al. (2020). Challenges in Specifying and Predicting Space Weather. *Space Weather*. https://doi.org/10.1029/2019sw002404

Tsagouri, I., Belehaki, A., Bergeot, N., Cid, C., Delouille, V., Egorova, T., et al. (2013). Progress in space weather modeling in an operational environment. *Journal of Space Weather and Space Climate*, *3*, A17. https://doi.org/10.1051/swsc/2013037

Vesnin, A. M. (2014). *Validation of F2 layer peak height and density of real-time international reference ionosphere (Master Degree Thesis)*. Lowell, MA, USA: Univ. of Massachusetts Lowell. Retrieved from https://ulcar.uml.edu/GAMBIT/Vesnin-Master-thesis-2014.pdf

Wahba, G. (1990). *Spline models for observational data*, *CBMS-NSF Regional Conference Series in Applied Mathematics* (CB59 ed.). Philadelphia, Pennsylvania: Society for Industrial and Applied Mathematics (SIAM). https://doi.org/10.1137/1.9781611970128

Wu, Z., Huang, N. E., Long, S. R., & Peng, C. K. (2007). On the trend, detrending, and variability of nonlinear and nonstationary time series. *Proceedings of the National Academy of Sciences*, *104*(38), 14,889–14,894. https://doi.org/10.1073/pnas.0701020104